

## Flow-Imaging of Convective Geothermal Systems – Obtaining Seismic Velocity Models Needed for Production Well Targeting

P Leary, P Malin, G Saunders, T Fleure, C Sicking, S Pullammanappallil  
Geoflow Imaging Ltd, Auckland 1010, New Zealand  
[peter@geoflowimaging.com](mailto:peter@geoflowimaging.com); [graeme@geoflowimaging.com](mailto:graeme@geoflowimaging.com)

**Keywords:** geothermal energy, geothermal drilling, crustal fractures, crustal flow, fracture imaging, refraction seismics

### ABSTRACT

We discuss acquisition of seismic velocity models needed to use passive seismic data to locate drilling targets in convective geothermal flow systems. The requisite models are derived by applying Fast Marching computation to observed travel time data between wellbore sources and surface sensors.

"It is a truth universally acknowledged" (Austen 1813), that well drilling uncertainty and risk is stalling growth of geothermal power production. The high flow demand of turbines combined with high spatial erratics in crustal flow systems creates high initial risks that paralyse geothermal project decision-making. As a remedy, we propose that multi-channel seismic data acquisition and processing proven for shale formation O/G production can image the erratic flow structures of convective geothermal systems in volcanic terrains.

We assess the current impasse by first noting that crustal reservoir flow systems are spatially erratic at all scale lengths. Spatially-correlated crustal porosity  $\phi(x,y,z)$  leads to poro-connectivity percolation clustering at all scales to generate the permeability empiric  $\kappa(x,y,z) \sim \exp(\alpha\phi(x,y,z))$ . The value of the constant  $\alpha$ , fixed by the observation that  $\alpha\phi \sim 3-4$  for a wide range of crustal flow systems, guarantees that crustal well productivity is lognormally distributed. Lognormal distributions are consistent with flow observations for active and fossil geological flow systems worldwide.

While hydrocarbon production pay can cover drilling costs across the entire lognormal productivity range, only the few high-flow wells can do so for convective geothermal systems. All other geothermal wells are sunk costs. On a well-by-well basis, geothermal well pay is given by resource temperature  $T$  and flow velocity structure  $V$ ,  $Q \equiv \rho CTV$ . The smoothly varying temperature field  $T$  can be remotely estimated to spatial resolution of 500m-1km. To date, however, there is little or no ability to remotely estimate flow structures  $V$  at 500m-1km spatial resolution, let alone achieve a nominal 50m spatial resolution needed to enable cost-effective production well drilling.

It is thus essential for future convective geothermal development to apply new technologies to locate high fluid flow clusters at  $\sim 50$ m resolution in advance of costly exploration drilling. Proven shale formation flow imaging technology at 25m resolution proceeds via acquisition of standard surface seismic reflectivity velocity models. Adapting the demonstrated flow imaging technology to convective geothermal systems reduces to acquiring an adequate seismic velocity model of the target crustal volume. Velocity model data acquisition for a 3km x 3km x 2km volume of volcanic terrain can proceed via seismic refraction travel-times from downhole sources to  $\sim 1000$  surface sensors. Downhole seismic source energy can be safely and reliably provided by deflagration burns of propellant charges of 30MJ (energy equivalent to a 2000 cubic inch marine airgun). Embedding the observed travel-time data in a 100 x 100 x 100 node target volume model at 30m spatial resolution allows accurate computation of travel-times for a large range of nominal target volume source points to surface array sensors. As demonstrated by active flow imaging at 15-25m for shale formations, such a travel-time table accurate to 30m applied to convective geothermal flow systems is sufficient to process ambient seismic listening data from surface sensor arrays into reliable images of convective geothermal flow structures for production well targeting.

### 1. INTRODUCTION

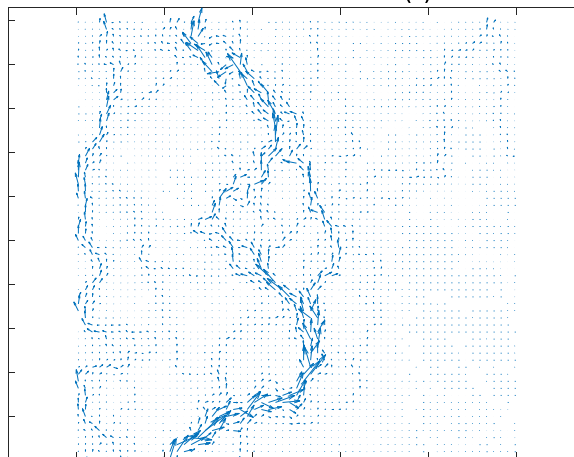
Fluids flow in the earth's crust via spatially erratic and unpredictable fracture-connectivity pathways at all scale lengths. Drilling access to significant crustal flow systems is therefore chancy, as noted by Slichter (1905) in an account of USGS groundwater surveys in California and elsewhere in the United States:

*It does not count against the above statements concerning the ability to determine in advance the probable yield of a well to find that neighboring wells, similarly constructed, yield very different amounts of water, or that water can not be obtained a short distance from a good well. Such a discovery always causes considerable comment, while the numerous cases in which ground water is found at very uniform depths and in nearly identical material call forth no comment whatever.*

Well production of all crustal fluids -- groundwater, conventional and unconventional hydrocarbons, convective geothermal systems, fossil flow mineral depositions -- is now generally known to lognormally distributed, meaning that a minority of wells produce a majority of fluid while a majority wells produce a minority of fluid (e.g., Malin et al 2015; Leary et al 2018).

Crustal fluid pathway erratics leading to lognormal well production distributions are traceable to a trio of essentially universal empirics: (i) crustal porosity spatial fluctuations recorded by well-logs are spatially correlated at all scales according to the spectral power-law  $S(k) \sim 1/k$ ,  $1/\text{km} < k < 1/\text{cm}$  (Leary 2002); (ii) crustal permeability  $\kappa$  is controlled by crustal porosity  $\phi$  as recorded by well-core sequences  $\delta \log(\kappa_n) \sim \delta \phi_n$ ,  $n = 1 \dots N$  (Leary et al 2018); and (iii), the relation  $\kappa(x,y,z) \sim \exp(\alpha\phi(x,y,z))$  in which the parameter  $\alpha$  is observed to obey the condition  $\alpha\phi \sim 3-4$  for mean formation porosities  $\phi$  across the range  $0.1\% < \phi < 30\%$  (Leary et al 2017, 2018).

Empirics (i)-(iii) are observed to impact the spatial and magnitude distribution of crustal microseismicity. Recently acquired deep crustal microseismicity data demonstrate that fluid-induced seismic slip event magnitude and event location distributions are highly influenced by ambient crustal permeability. Induced seismicity Gutenberg-Richter (G-R) moment distributions are explicitly lognormal rather than power-law (Leary et al 2020), and the spatial correlation of microseismic events  $\Gamma_{\text{meq}}(r) \sim 1/r^n$ ,  $n \sim 1/2$  is a power-law congruent with the spatial correlation properties of crustal permeability (Leary et al 2019). The evidence for a lognormal G-R relation in crustal seismicity has been widely observed but has been in deference to the traditional G-R relation as a power-law scaling fractal, the evidence has been systematically viewed as an observational deficiency rather than an ambient crustal property. In parallel, the power-law two-point spatial correlation property of microseismicity  $\Gamma_{\text{meq}}(r) \sim 1/r^{1/2}$  is readily observed in existing microseismicity catalogs but has not been identified or commented on.



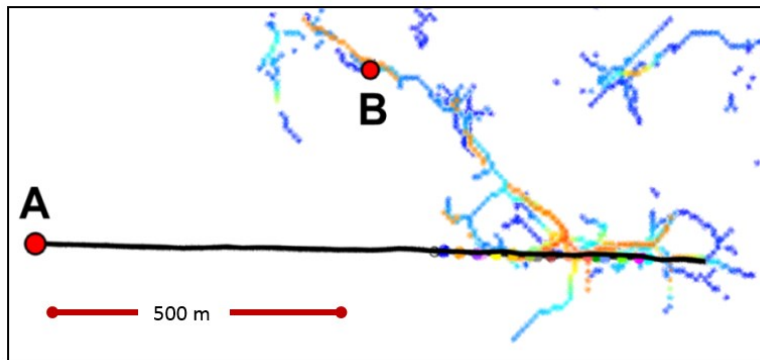
**Figure 1: Illustration of fluid-flow channels from spatially-correlated porosity distributions  $\phi(x,y,z)$  in the ambient crust. Pore-scale connectivity structures create permeability structures  $\kappa(x,y,z) \sim \exp(\alpha\phi(x,y,z))$  for observed values of parameter  $\alpha$  meeting empirical condition  $\alpha\phi \sim 3-4$ . Lognormal wellbore productivity in geothermal flow systems arises from such flow channelling (cf. Leary et al 2017, 2018 and Figs 2-3).**

Figure 1 illustrates effect of crustal flow structure empirics (i)-(iii). Spatially-correlated porosity distributions given by empiric (i) can generate localised poro-connectivity channels according to empiric (ii) for values of poro-connectivity parameter  $\alpha$  given by empiric (iii),  $\alpha\phi \sim 3-4$  (Leary et al 2018). In accord with observed lognormal distributions, drilling into the Figure 1 flow structure produces little fluid unless drilling intersects the flow channel denoted by flow velocity arrows.

While crustal microseismicity is seen to be loosely connected to crustal fluid flow empirics (i)-(iii), Figs 2-3 establish the existence of a much more integrated observational connection. The two figures illustrate how detection of very small but temporally-persistent, spatially-connected seismic emissions can reliably track fluid-flow fracture connectivity pathways in shale formations. First presented by Geiser et al (2012) for stimulated shale formations, Lacazette et al (2013) and Sicking et al (2016, 2017) show that flow-sourced seismic emissions can be passively mapped in the ambient crust in advance of fluid stimulation.

Figs 2-3 each show a plan view of a horizontal shale formation embedded with a long-reach production well (black lines). The coloured elements of the plans mark the location of ‘‘voxels’’ (numerical grid volume elements) within the shale formation identified as persistent emitters low-level seismic energy.

In Figure 2, each shale formation voxel of 10m dimension is color-coded according to the relative size the acquired seismic emission signal. The spatial distribution of seismic emitter voxels clearly resembles a fracture-connectivity structure. The marked seismic emission voxel locations are seen to be related to shale formation fluid flow structures in the sense that when well A fluid was injected into the formation at the positions of the intersection of the well and the voxel structure, fluid appeared in well B that had no prior observed connection to Well A. Well A fluid injected at intervals not intersecting the voxel structure did not reach well B.



**Figure 2: Plan view of horizontal Marcellus shale formation transected by wells A and B. Well A has a long horizontal leg in the shale formation (black line). Well B had no known connection to Well A. Colourised voxels denote shale locations where passive seismic data indicate the presence of low-level seismic emissions. During systematic stimulation of Well A, fluid injection at the points of intersection with the seismic-emission structure caused Well B to flow. (Lacazette et al 2013)**

In Figure 3, the left-hand image black shading marks voxels with above-threshold seismic emission levels observed prior to fluid stimulation of the embedded production wellbore. The middle image blue shading marks regions of the post-stimulation shale formation in which fluid flows into the production wellbore. The right-hand image overlays the left-hand and middle images.

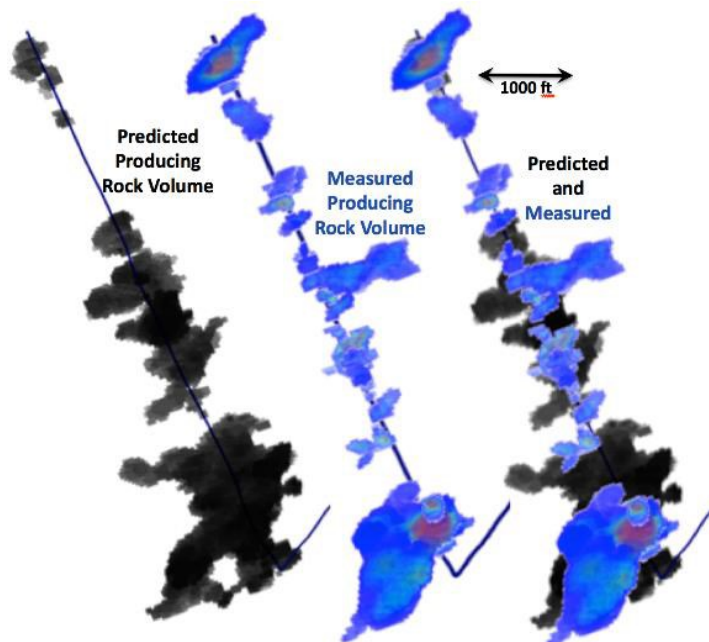


**Figure 3: Three-image plan view of horizontal New Albany shale formation drilled by a horizontal-reach production well with short vertical reach at lower right (black line). (Left) Active voxel distribution pre wellbore stimulation/fracking. (Middle) Active voxel fluid flow distribution post stimulation/fracking. (Right) Overlay of pre- and post-fracking images. (Sicking et al 2016)**

The Figure 1 conceptual understanding of how spatially erratic and unpredictable crustal flow pathways define crustal permeability allows us to interpret Figure 2-3 images as maps of low-level microseismicity generated by crustal fluids flowing

Leary et al.

through crustal permeability structures. Joining crustal flow empirical concepts to array seismic observation of detailed crustal flow structures offers a new practical perspective on crustal reservoir operations that is particularly relevant to power production from convective geothermal systems.

## 2. THE PRINCIPLE OF SURFACE SENSOR RECORD STACKING TO LOCATE SUBSURFACE SPATIOTEMPORAL EMITTERS

We interpret Figs 2-3 in terms of crustal flow structures simulated in Figure 1: Continuous fluid flow along long-range spatially-connected ambient poroperm distributions generate quasi-coherent *time-persistent spatially-localised seismic emissions* along naturally-occurring, ever-present fracture-connectivity pathways.

We know from deep-crust field evidence of rock responding to injected fluids that fluid flow stimulates detectable seismic slip events that accord with the permeability structure of the field-scale activated volume (Kwiatek et al 2019; Leary et al 2020). It is well attested at laboratory and mine scale that crustal rock fracture structures persist to the grain scale (e.g., Hirata et al 1987). We can, therefore, robustly expect that crustal fluid-injection induces seismic emissions across the full range of scales. In consequence, low-level seismic emissions associated with persistent crustal fluid flow localised in subsurface spatially-correlated fracture-connectivity structures can be expected to emerge from a suitable stacking procedure applied over a suitable length of time across a suitable array of surface sensors.

The seismic emission signal stacking procedure is based on a suitably accurate seismic velocity model of the crustal survey volume. Temporally persistent seismic emissions from a stable localised spatially-connected fluid flow structures will be embedded in the seismic noise recorded by an array of  $N_{\text{sns}}$  surface seismic sensors. The known seismic velocity structure of the embedding crustal volume is coded in a seismic travel-time cross-table  $TT(I,J)$  connecting every subsurface voxel,  $I=1 \dots N_{\text{vox}}$ , to every surface sensor,  $J=1 \dots N_{\text{sns}}$ .

With  $N_{\text{vox}} \times N_{\text{sns}}$ -entry travel-time cross-table  $TT(I,J)$ , it is possible to systematically stack temporal sequences of seismic sensor data by time-shifting each of  $N_{\text{rec}}$  sensor record windows of each of  $N_{\text{sns}}$ . The  $N_{\text{rec}} \times N_{\text{sns}}$  time-shift operation is applied to each of  $N_{\text{vox}}$  voxels so that a persistent emission signal arising in any given voxel effectively arrives at the start of each of  $N_{\text{rec}} \times N_{\text{sns}}$  sensor records. Voxels that are steady seismic emitters in time and space will generate coherent signal stacks of  $N_{\text{rec}} \times N_{\text{sns}}$ -fold. Voxels that do not emit temporally or spatially consistent signal will not generate a coherent signal stack. The largest and steadiest of the  $N_{\text{vox}} \times N_{\text{rec}} \times N_{\text{sns}}$ -fold seismic stacks are logically due to significant flow-active voxels in the shale formation.

Figs 2-3 are two of many examples of spatial congruence of low-level seismic emission processing images with independence evidence of fracture-connectivity fluid flow in frack-stimulated shales. The seismic emission images and the fluid-flow systematics are consistent with the empirics of crustal flow systems and associated microseismicity enumerated above. It is logically consistent to expect that fluid flow systems associated with convective geothermal fields follow the same underlying physics and will support the same image production as producing shale formations. The essential difference between shale formation flow structure imaging and convective geothermal flow structure imaging is that convective geothermal flow systems are embedded in disordered volcanic terrains rather than ordered sedimentary terrains. Seismic reflectivity methods that generate comprehensive and robust seismic velocity models of ordered shale formation crustal sections fail to image disordered volcanic terrains. To bring seismic emission imaging to convective geothermal fields requires a methodology for acquiring seismic velocity models of the appropriate crustal volumes. The following sections address such a velocity model procedure for convective geothermal systems in volcanic terrains.

## 3. ACQUIRING A SEISMIC VELOCITY MODEL FOR CONVECTIVE GEOTHERMAL FLOW SYSTEMS

Figure 4 offers a quick visual fix on the stratigraphic order/disorder contrast of a sedimentary deposit sequence (above) and a pyroclastic flow sequence (below) in views that are respective NW versus SE across the Rio Grande River plain in the Creede mining district Oligocene eruptive complex. The sedimentary sequence reflects seismic waves in an orderly fashion, while the ash flow tuff scatters seismic waves in a disorderly fashion.

Failure of plane wave reflection seismometry for disordered pyroclastic ash flow tuffs and similar lava terrains requires that refraction seismometry be applied to convective geothermal systems (Telford et al 1984). Standard refraction seismometry via surface-source-to-surface sensor geometry poses, however, an acquisition problem: travel paths reaching 2km depths require source-sensor offsets of order 10km. Fortunately, the 2km-deep wellbores central to convective geothermal system operations permit using a wellbore-to-surface seismic sourcing geometry with surface arrays of dimension 2-3km.



**Figure 4: Views of layered alluvium (above) and pyroclastic-flow tuff (below) across the Rio Grande River, Creede mining district eruptive complex, Colorado.**

An appropriate downhole seismic energy sourcing means has been established by recent attempts to stimulate geothermal wellbores via deflagration-burn gas pressurisation with rise times of order 0.01-0.1 ms (Sigurdsson 2015; Wieland et al 2006). Safe, low-cost, high-temperature stable deflagration burns can now provide wellbore-friendly bubble oscillations of order 30MJ compressive energy in wellbore fluids at 1-2km depths appropriate to most convective geothermal systems.

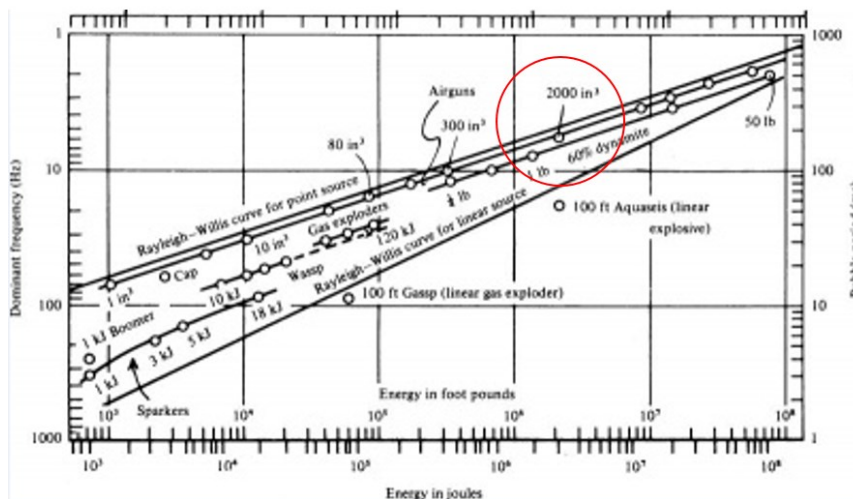


**Figure 5: Rayleigh-Willis underwater explosion bubble oscillation frequency for range of energies and confining pressure depths. A 2000 cubic inch marine airgun releases 30MJ energy equivalent to experimental propellant energy release in geothermal wellbores. [wiki.seg.org/wiki/Dictionary:Rayleigh-Willis\\_relation](http://wiki.seg.org/wiki/Dictionary:Rayleigh-Willis_relation)**

Figure 5 compares 30MJ bubble-source energy levels to the performance scale of standard marine airguns. The approximate bubble oscillation frequency in open water is  $F \sim 10(D+10)^{5/6}/E^{1/3}$  for bubble energy  $E$  in Joules at confining pressure in meters of water depth  $D$  (Landrö 2014). In open water,  $E \sim 30MJ$  at 2km depth,  $F \sim 20Hz$ . For bubble oscillations confined to a wellbore, the frequency is  $\sim$  double that for open water. This seismic source frequency range is comparable to the observed range of shale formation stimulation seismic emission signals processed for Figs 2-3 and related flow structure images.

Based on presently available propellant performance data, it appears entirely practical to generate the requisite suite of seismic travel time data for crustal volumes of order 2-5km x 2.5km x 2.5km as diagrammed in Figure 6.

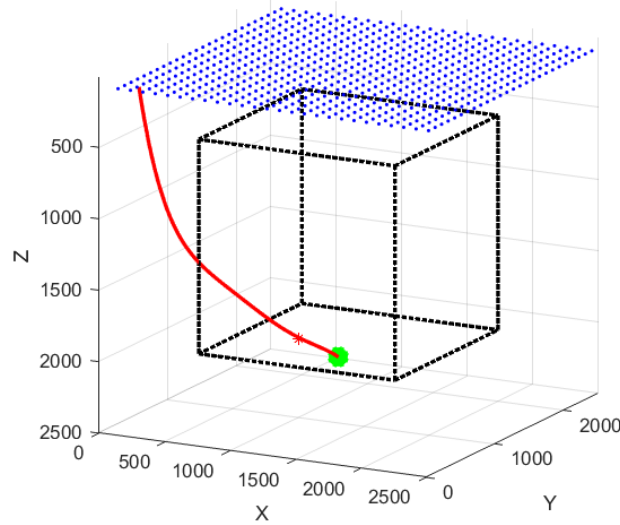


**Figure 6: Schema of wellbore-based propellant-charged seismic refraction travel-time survey of a convective geothermal crustal volume 2.5km on a side. Red line is geothermal wellbore; green dot is seismic wave from wellbore source; blue dots are surface array seismic sensors recording wellbore-sourced wavefield; black dotted box is effective crustal survey volume; red asterisk is a nominal survey grid voxel for which survey volume travel-times to surface sensors are to be estimated from wellbore-source travel-time data. The measured source-to-sensor travel-times are termed  $TT(0,J)$ ,  $J=1\dots N_{sns}$ ; the sought travel-times are termed  $TT(I,J)$ ,  $I=1\dots N_{vox}$ ,  $J=1\dots N_{sns}$ .**

The elements of Figure 6 crustal volume are the surface sensor array (blue dots), wellbore (red line), source seismic pulse (green dot), domain of gridded seismic emission voxels associated with the active convective geothermal flow system (black dotted lines), and putative seismic emission voxel within the refraction seismic survey domain (red asterisk). The wellbore seismic source radiation field recorded by the surface sensor array provides a set of seismic refraction surface-sensor travel-time data  $TT(0,J)$ ,  $J=1\dots N_{sns}$  originating at the wellbore. Given these refraction-survey travel-time data, we seek to estimate travel times to surface sensors,  $TT(I,J)$ ,  $I=1\dots N_{vox}$ ,  $J=1\dots N_{sns}$ , for all red asterisk voxels within the black dotted lines. §4 discusses how Figure 6 wellbore-sourced surface seismic array travel-time data  $TT(0,J)$ ,  $J=1\dots N_{sns}$ , are processed to provide the crustal seismic velocity travel-times  $TT(I,J)$ ,  $I=1\dots N_{vox}$ ,  $J=1\dots N_{sns}$  needed for flow imaging.

#### 4. PROCESSING WELLBORE-TO-SURFACE SEISMIC TRAVEL TIME DATA FOR SEISMIC EMISSION SOURCE IMAGING

Figs 2-3 imaging of low-level flow-structure seismic emissions in shale formations is proceeds via a seismic travel-time cross-table  $TT(I,J)$  connecting  $I=1\dots N_{vox}$  subsurface voxels to  $J=1\dots N_{sns}$  surface sensors. The travel-time cross-table  $TT(I,J)$  for sedimentary crustal volumes is provided by velocity models given by standard reflection seismic methods. We now explore how cross-tables  $TT(I,J)$  can be estimated from wellbore-to-surface seismic travel-time data  $TT(0,J)$  acquired for a convective geothermal flow system as illustrated in Figure 6.

We first use a simple velocity field to illustrate the parameter search procedure that seeks to derive cross-table travel times  $TT(I,J)$  from wellbore-to-surface sensor travel times  $TT(0,J)$ . The procedure is seen to output velocities fields from input velocity fields given by smoothly varying x-, y- and z-velocity gradients embedded in ambient white-noise random noise fluctuations of order 2% rms fluctuation amplitude. For such simple input velocity fields, the search algorithm can return output velocity fields having close approximations to the gradients of the input velocity field. The search algorithm can be generalised to a two-layer crustal velocity structure involving two sets of velocity gradients, as might be used to represent a complex surface layer overlying an ambient crustal velocity field. Ability to use white noise velocity fields to recover output velocity fields providing close approximations to the input velocity model gradients is proof that the output velocity field is a good representation of the input velocity field, and will suffice to process surface seismic sensor records to image subsurface seismic energy emitters.

We then show that the parameter search algorithm produces adequate results for crustal volumes with velocity fields for which x-, y- and z-velocity gradients are embedded in 1/k-scaling spatially-correlated random noise of 6 RMS fluctuation amplitudes as is observed

in sonic well-log data worldwide. While the fitting process for the simple low-noise input velocity fields converges strongly to the input velocity gradients, noisy  $1/k$ -scaling spatially correlated input velocity fields allow adequate approximations to the input velocity field, but do not converge to accurate evaluation of input model gradients. To validate the travel-time inversion process for 6% spatially-correlated ambient crustal velocities fields we need to conduct simulations of the signal stacking process.

The point here is that, while refraction seismic data  $TT(0,J)$  for a realistic input velocity field cannot converge to a complete point-by-point output velocity field, the fitting algorithm can produce an adequate table estimate  $TT_{est}(I,J)$  from realistic  $TT_{est}(0,J)$  refraction travel-time data if the goodness-of-fit is relaxed to a more functional criterion. The relaxed goodness-of-fit criterion does not attempt to duplicate the input velocity gradients, but is rather defined as the ability of the search algorithm's output velocity field to adequately reproduce seismic emission voxel locations computed for the input velocity field. This goodness-of-fit criterion is precisely what we expect to achieve for convective geothermal system imaging.

The following steps itemise the procedure for estimating cross-table travel-times  $TT_{est}(I,J)$  from 'actual' wellbore-to-surface sensor travel times  $TT_{act}(0,J)$  computed for simulations of 'actual' crustal velocity fields  $V_{act}$  as illustrated in Figure 6:

- a. Generate velocity field  $V_{act}$  to represent the seismic velocity structure of a 2.5km x 2.5km x 2.5km crustal convective geothermal system;
- b. Use  $V_{act}$  to compute simulated field-observed wellbore-to-sensor-array travel times  $TT_{act}(0,J)$ ;
- c. Generate trial velocity fields  $V_{est}$  and compute trial travel-times  $TT_{est}(0,J)$ ;
- d. Compare  $TT_{est}(0,J)$  to  $TT_{act}(0,J)$ ;
- e. Modulate trial velocity field parameters so that successive trial travel-times  $TT_{est}(0,J)$  adequately match actual travel-times  $TT_{act}(0,J)$ ;
- f. Use fit-estimate velocity field to compute cross-table  $TT_{est}(I,J)$ ;
- g. Compare  $TT_{est}(I,J)$  to  $TT_{act}(I,J)$  to get the range and distribution of travel-time errors;
- h. Perform signal stacks for a range of seismic emitter voxel locations  $I = 1 \dots N_{vox}$  to validate  $TT_{est}(I,J) \sim TT_{act}(I,J)$  condition.

We first illustrate  $TT_{est}(I,J) \rightarrow \sim TT_{act}(I,J)$  estimation with low-amplitude uncorrelated random noise velocity fields, then give results for velocity fields with more realistic degrees of spatial noise correlation and amplitude. The velocity fields are represented by 100 x 100 x 100 node arrays at 25m spacing in the geometry of Figure 6. The surface sensor array is either 26 x 26 (676 sensors at 100m spacing) or 51 x 51 (2601 sensors at 50m spacing). Travel-time computations across the velocity fields are performed with a scalar Fast Marching Method (FMM) procedure implemented in Matlab. FMM computation accuracy is validated against acoustic wave propagation computations; computational speeds are 30 to 100 times faster for 100 x 100 x 100 and 200 x 200 x 200 node velocity fields.

Characterising the crustal velocity field is an open-ended matter. To keep the characterisation bounded, we employ three generic features of upper-crustal seismic velocity fields. First, seismic velocities tend to increase with depth. Second, the velocity increase with depth is often adequately approximated by a linear trend ( $V \sim 1 + gZ$ ), but parabolic ( $V \sim \sqrt{1 + gZ}$ ) and fractional-power-law ( $V \sim (1 + gZ)^{1/n}$ ) trends have also been applied (Greenhalgh & King 1981). Third, well-bore sonic logs are universally characterised by  $1/k$ -scaling random fluctuation-power distribution in the range of 6% root-mean-square amplitude (Leary 2002). Building on these generic crustal velocity characteristics, it is logical to allow for lateral trends as well as vertical within in the random background velocity fields. Our present generic (isotropic) computational velocity fields are thus represented by a minimum and a maximum velocity, with linear gradients in x-, y-, and z-directions superposed on a background random velocity fluctuation field.

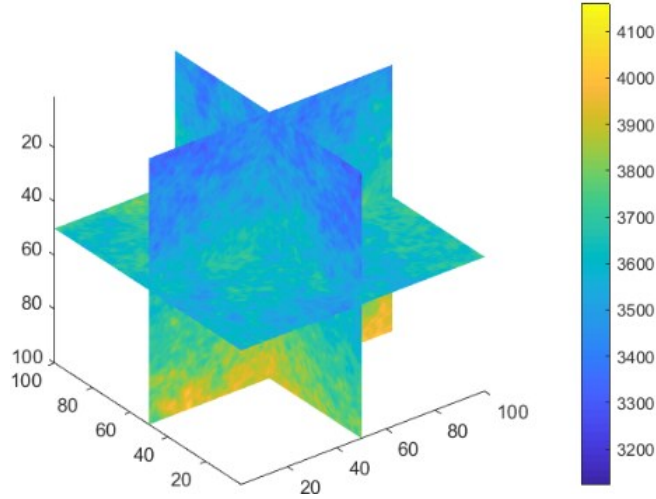
If the random background velocity field is uncorrelated, then spatial averaging over hundreds of nodes along any given travel path is apt to be independent of any given set of random numbers, and the modelling process is quite robust and convergent. Our first velocity-inversion modelling presentation is for uncorrelated randomness. As in actuality the random fluctuations of crustal velocities are spatially correlated, it follows that representations of actual crustal velocity field should be spatially correlated. A logical case can then be made that trial random crustal velocity fields should also be spatially correlated. We have followed this logic in the second inversion modelling presentation.

Our results indicate that for the present set of velocity fields, it is possible to estimate the travel-time cross-table  $TT_{est}(I,J)$  to within a few milliseconds of the actual cross-table  $TT_{act}(I,J)$  for a central range of voxel locations as indicated by the dotted box in Figure 6, and to within 3-5 milliseconds within most of the entire computational volume of Figure 6.

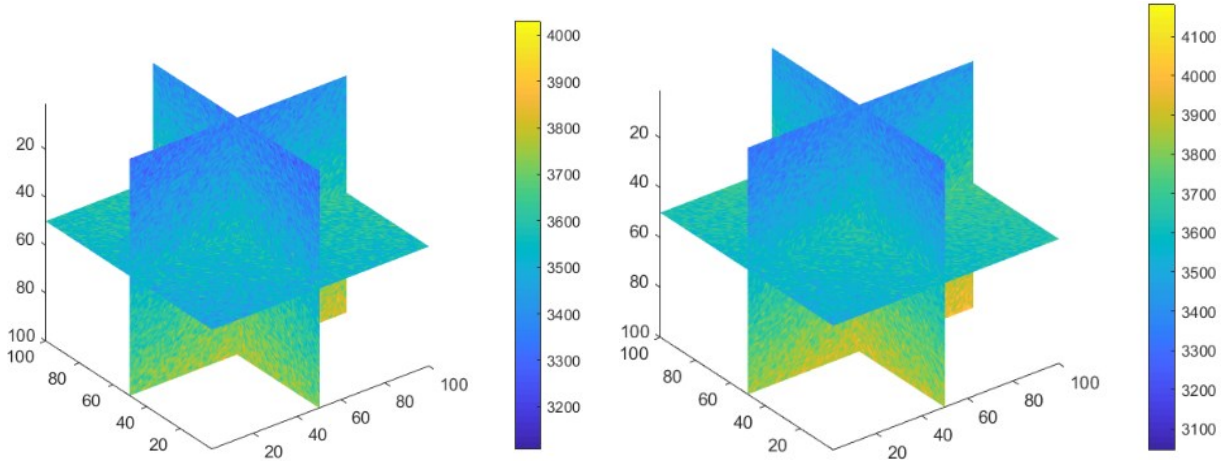
#### 4.1 Inverting wellbore refraction data reduced-noise velocity fields with x-, y-, z-gradients embedded in uncorrelated random noise volumes

Figure 7 shows a 100 x 100 x 100 node numerical seismic velocity field in the geometry of Figure 6 as realised according our set of generic properties of crustal velocities: spatially correlated randomness according to the spectral power-law scaling empiric  $S(k) \sim 1/k$ ,  $1/km < k < 1/m$  with linear velocity trends in x-, y-, and z-directions. The rms amplitude of spatial fluctuation is  $\sim 2\%$ . Figure 8 shows initial (left) and final (final) estimated velocity fields constructed of spatially uncorrelated random noise with an initial trio of gradient parameters (left) and final trio of gradient parameters (right). Figure 9 compares the 'actual' travel-time distribution (blue traces) computed for the Figure 6 source-sensor geometry with 'estimated' travel-time distributions (red traces) for the initial trial gradient-set

(upper panel) and final trial gradient-set (lower panel). Figure 10 shows the spatial distribution of velocity field fit residuals. It is evident that the travel-time estimate procedure converges to the “actual” travel-times for low amplitude white noise fluctuations.



**Figure 7:** A 100x100x100 node seismic velocity structure of ambient crustal volume 2.5km on a side. Velocity fluctuations are controlled by spatially-correlated porosity field  $\phi(x,y,z)$  that in turn creates permeability field  $\kappa(x,y,z) \sim \exp(\alpha\phi(x,y,z))$ ; vertical and lateral velocity gradients are superposed on the fluctuation field. Velocity fluctuations have 2% rms amplitude. The given velocity field represents an “actual” geothermal crustal velocity field that generates source-to-sensor travel times  $TT_{act}(0,J)$ . We seek to construct a numerical field having approximately the same source-to-sensor travel  $TT_{est}(0,J) \sim TT_{act}(0,J)$ .



**Figure 8:** Initial (left) and final (right) trial velocity fields used to estimate the Figure 7 velocity field in terms of a white-noise fluctuation field with good estimates if the actual x-,y-,z- velocity gradients. As seen in Figure 9, the right-hand velocity field travel-times are good estimates of the “actual” travel-times,  $TT_{est}(0,J) \sim TT_{act}(0,J)$ , leading to good estimates of cross-table travel-times,  $TT_{est}(I,J) \sim TT_{act}(I,J)$ ,  $I = 1 \dots N_{vox}$ .

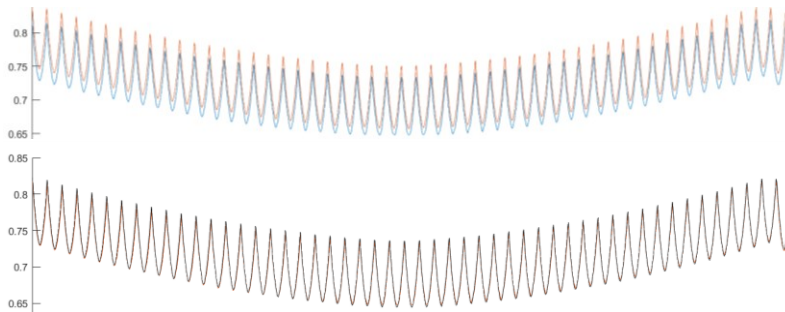


**Figure 9:** Overlays of  $TT_{est}(0,J)$  in red and  $TT_{act}(0,J)$  in blue for initial/final trial velocity fields (above/below).

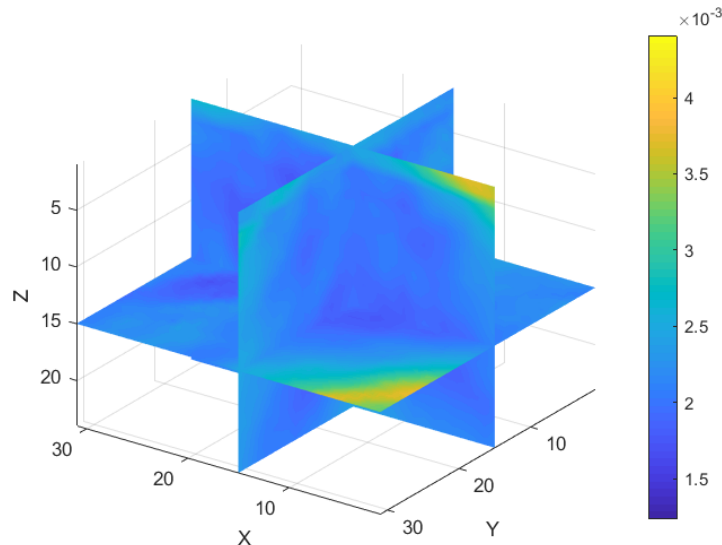


**Figure 10: Spatial distribution of residual travel-times  $TT_{\text{est}}(I,J) - TT_{\text{act}}(I,J)$ ; the mean residual is  $\sim 2\text{msec}$ .**

Figure 10 displays the spatial distribution of mean voxel-to-sensor travel-time error between the ‘‘actual’’ and the ‘‘estimated’’ velocity fields for 961 50m voxels spanning the Figure 6 dotted volume. The mean and standard deviation of travel-time errors is  $2.1 \pm 0.3$  msec. At this level of temporal fidelity, each 50m voxels in the centre of the survey volume is spatially located with  $\sim 10\text{m}$  accuracy relative to the sensor array; i.e.,  $TT_{\text{est}}(I,J) \sim TT_{\text{act}}(I,J)$ . Seismic emissions from any ‘‘actual’’ voxel recorded during a field survey will thus be reliably assigned to the correct source voxel location via the ‘‘estimated’’ voxel cross-table, and will contribute to a signal stack over  $N_{\text{rec}}$  data record intervals across the array of  $N_{\text{sns}}$  sensors.

#### 4.2 Inverting wellbore refraction data for ambient-noise velocity fields with x-, y-, z-gradients embedded in correlated random noise volumes

Figs 7-10 demonstrate that there is no expectation or need for the estimated seismic velocity field to closely resemble the spatial fluctuations of ‘‘actual’’ seismic velocity field. All that is needed or expected is that the estimated and ‘‘actual’’ integrated refraction seismic travel-time cross-tables are similar,  $TT_{\text{est}}(I,J) \sim TT_{\text{act}}(I,J)$ .

When the crustal velocity spatial fluctuation noise rms amplitude increases to 6%, the sensitivity of the gradient-parameter search is reduced, and the estimation process becomes dependent on the trial ambient spatial fluctuation field as much as on the velocity gradients. We thus turn to trial estimation velocity fields that are generically compatible with the empirical  $S(k) \sim 1/k$  power-law scaling spatially correlated fluctuation field of the actual crust. The necessary and sufficient condition  $TT_{\text{est}}(I,J) \sim TT_{\text{act}}(I,J)$  still applies, but the structure of ambient random spatial correlations is now taken into account.

Figures 11-13 summarise a computation in which the trial estimation velocity field spatial correlations match those of the ambient crust. Figure 11 reprises Figure 7 for the case that  $1/k$ -scaling spatial correlations are realised for a greater range of seismic velocity but with less evident velocity gradients. Figure 12 (left) reprises the Figure 8 (left) distribution of the differences between ‘‘actual’’ and estimated velocities when the trial velocity fields are now pink noise ( $1/k$ -scaling) instead of white noise. Figure 12 (right) reprises Figure 10, giving the distribution of  $\text{mean}(TT_{\text{est}}(I,J)) - \text{mean}(TT_{\text{act}}(I,J))$ , the mean differences across the sensor array  $J = 1 \dots N_{\text{sns}}$  for the estimated and ‘‘actual’’ travel-times for source locations  $I = 1 \dots N_{\text{vox}}$ .

It is clear from Figure 12 (right) that there will likely be zones of substantial systematic misfit when the trial pink noise velocity field disagrees substantially from the ‘‘actual’’ pink noise velocity field. These zones of high-value travel-time misfit are, however, self-declaring, and can be managed out of the interpretation process by using several velocity field estimates instead of seeking a single ‘‘true’’ estimate. If the zone of high-value travel-time misfit is persistent across a number of estimates velocity field fits, then it can be concluded that the ‘‘actual’’ velocity field is itself anomalous. In the case of an anomalous ‘‘actual’’ velocity field, either the surveyed zone is removed from the interpretation process, or the survey is supplemented with additional observation.

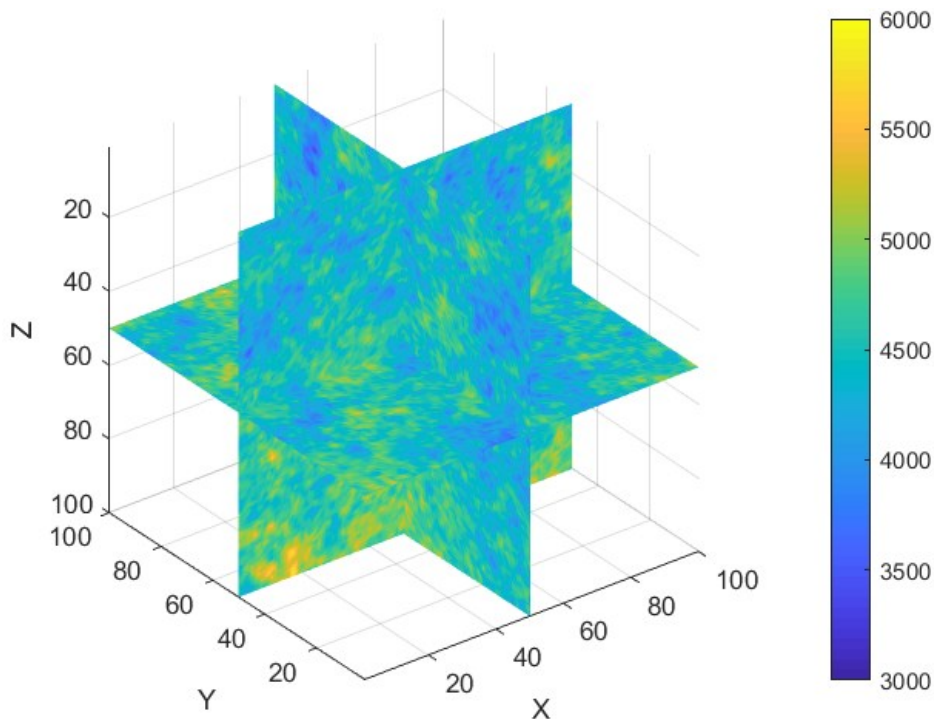


**Figure 11: Reprise of Figure 7 for velocity field fluctuations with 6% rms amplitudes.**

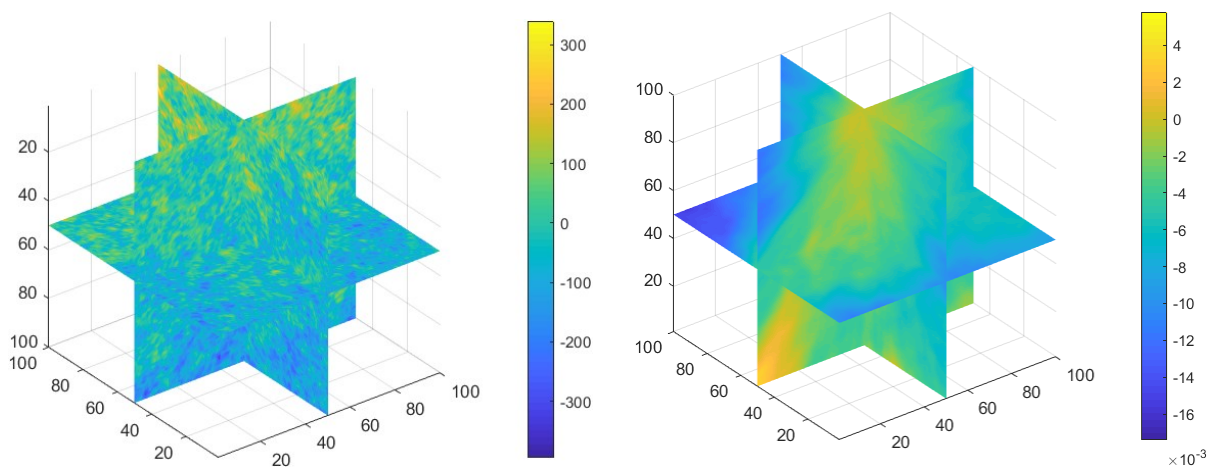


**Figure 12: (Left) Reprise of Figure 8 initial trial velocity field used to estimate the Figure 11 “actual” velocity field in terms of a  $1/k$ -scaling pink-noise fluctuation field. (Right) Reprise of Figure 10 residual travel-time field  $TT_{est}(I,J) - TT_{act}(I,J)$ ; expected residuals are of order 3-5 msec except at edges of computational volume.**

Figure 13 shows the travel-time misfit distribution for the Figures 11-12 case of pink-noise trial velocity fields for voxel locations confined to the central dotted volume shown in Figure 6. It is seen that while the travel-time misfits exceed those shown in Figure 10, the travel-time misfits are of order 4 msec, giving seismic emission source spatial resolution error of order 20m. Figure 14 then displays the result of using suitable estimation velocity cubes to locate nine instances of arbitrary source voxels denoted by the red asterisk within the “true” Figure 11 velocity cube. For each asterisk source location of travel-time cross-table  $TT_{true}(I,J)$ , six black circles denote a sequence of estimated positions for the source voxel derived from an estimated cross-table  $TT_{est}(I,J)$ . The best-fit black circles correspond to the actual source location with an effective accuracy of 1.3 nodes. The location procedure can be repeated for multiple estimated travel-cross tables  $TT_{est}(i,j)$  to strengthen the statistical certainty of the source location. The Figure 14 caption details the fitting procedure.

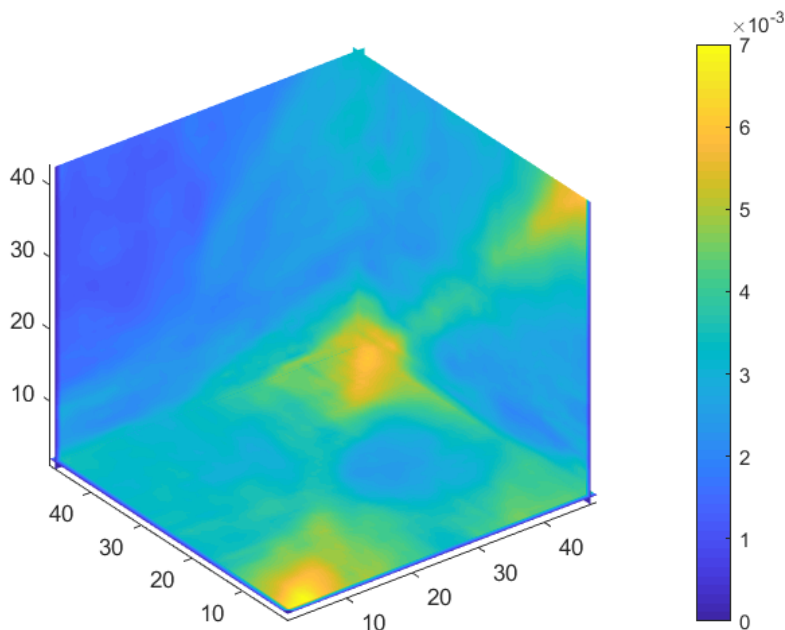


Figure 13: Reprise of Figure 10 for Figures 11-12 estimation of travel-time field residuals  $TT_{est}(I,J) - TT_{act}(I,J)$  for dotted box survey volume in Figure 6.

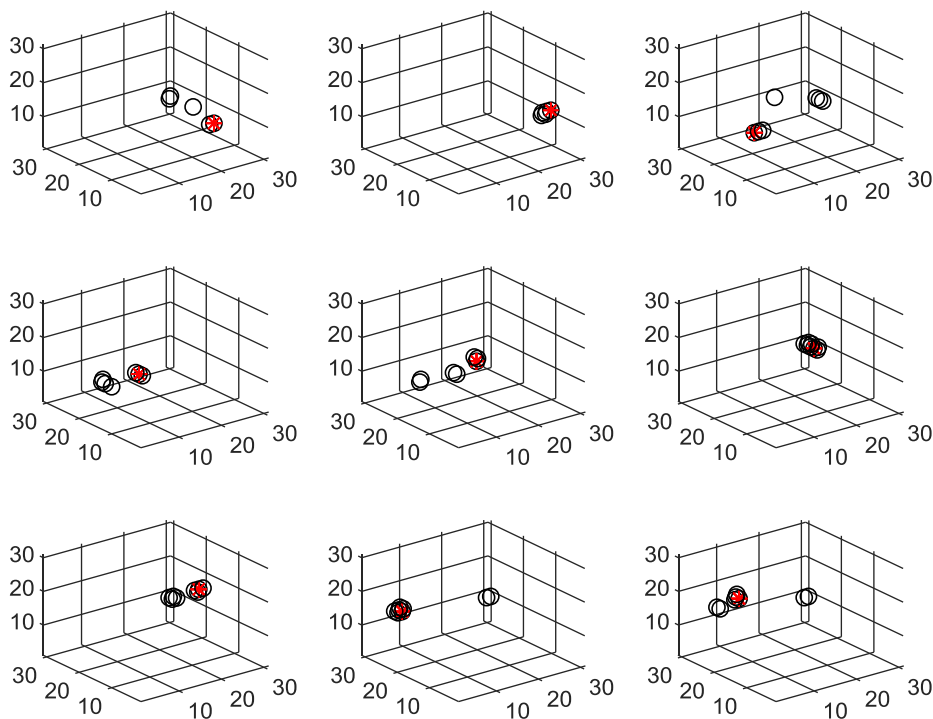
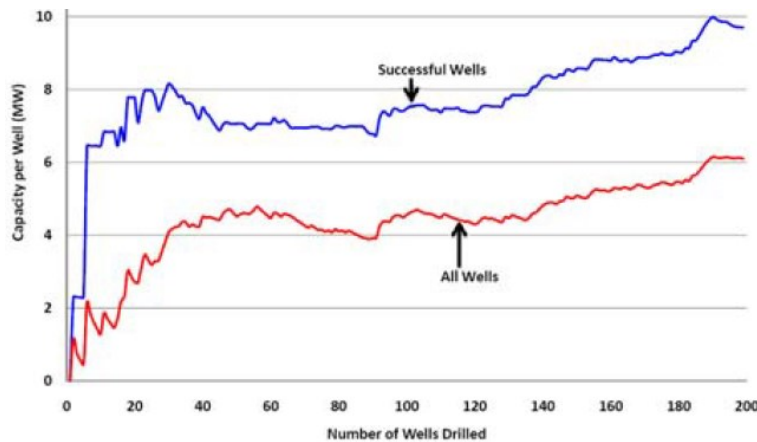


Figure 14 Display of source-voxel search algorithm performance. For the Figure 12 (left) ‘actual’ velocity field with source-sensor travel-time cross-table  $TT_{act}(I,J)$ , nine random source-voxel locations are selected,  $I_m, m = 1 \dots 9$ . For each selected source-voxel, the location  $I_m$  is identified by a red asterisk. Six values of estimated source positions  $1 \leq I_{est} \leq 6$  are plotted as black circles. The six  $I_{est}$  locations are those that most nearly minimise the travel-time-residual function  $\sum_{J=1 \dots N_{sns}} |TT_{act}(I_m, J) - TT_{est}(I_{est}, J)|$ . For each test voxel location  $I_m$ , the estimated source positions  $I_{est}$  with the smallest residuals successfully locate the test voxel. Estimated locations with higher residuals show the potential for source voxel location error. Performing the location search for several estimated travel-travel cross-tables  $TT_{est}(I,J)$  reliably reduces the statistical source-voxel location error. The statistical accuracy of estimated source-voxel locations is  $\sim 1.3$  nodes.

## 5. DISCUSSION/SUMMARY

On a well-by-well basis, geothermal well pay is given by resource temperature  $T$  and flow velocity structure  $V$ ,  $Q \equiv \rho CTV$ . The smoothly varying temperature field  $T$  can be remotely estimated to spatial resolution of 500m-1km. At present, however, there is no means of estimating either flow structures  $V$  at the 500m-1km spatial resolution of present field modelling, or, more importantly, at the nominal 50m spatial resolution illustrated in Figures 1-3 and simulated in Figures 6-14. Achieving these levels of spatial resolution for crustal flow structures could greatly reduce the exploration and/or production well drilling budget for both operating brownfield geothermal sites and assessing/developing greenfield geothermal sites.

Given the high flow demand of turbines ( $>100\text{MW}_{\text{th}}$ ) and the naturally occurring spatial erratics in convective geothermal flow systems discussed above, there are presently crippling risks associated with drilling either exploration wells or production wells. Figure 15 gives the average wellbore output  $Q$  MW as a function of number of wells drilled in Indonesia geothermal fields.



**Figure 15: Average wellbore output  $Q$  MW<sub>e</sub> as function of number of wells drilled in Indonesia geothermal fields (Sanyal et al 2011).**

In Figure 15, we see two aspects of lognormal distributions of crustal permeability and hence well productivity: (i) early drilling is inefficient as adequate flow-structure information is lacking; (ii) average well production for all wells is nearly 50% of average well production for ‘successful’ wells, i.e., nearly 50% of drilling expenditure is a ‘sunk cost’. Flow mapping surveys that identify crustal flow structures give prospects for (i) reducing/eliminating sunk costs; (ii) reducing/eliminating many or most of early stage drilling failures; (iii) enabling small field development through lowered drilling costs.

The high cost of drilling (USD3-5M for exploration wells and USD5-7M for production wells) is currently paralysing geothermal project decision-making. The multi-channel seismic data acquisition and processing proven for shale formation O/G production addresses the problem of imaging flow structures for convective geothermal systems in volcanic terrains. The inherent cost of deploying readily available 1000-sensor surface arrays, acquiring wellbore-sourced seismic refraction travel-time data, recording ambient seismic emission noise at the surface of convective geothermal flow system, and using the proven shale-formation data processing technology to generate a 2-3km-scale map of volumetric flow distribution at spatial 50m spatial resolution is of order USD500K. The prospective cost-reduction for an established field procedure to guide the convective geothermal drill bit to productive targets is thus of order USD50M/USD500K = 100. At this cost-reduction, present fields can be made more productive and more securely expanded and/or sustained, and a large number of prospective but now dormant greenfield sites can be explored and developed.

## REFERENCES

- Austen J (1813) *Pride and Prejudice*, T Egerton Publisher, Military Library, Whitehall, London.
- Geiser P, Lacazette A & Vermilye J (2012) Beyond ‘dots in a box’: an empirical view of reservoir permeability with tomographic fracture imaging, *First Break*, v. 30, p. 63-69.
- Greenhalgh SA & King DW (1981) Curved raypath interpretation of seismic refraction data, *Geophysical Prospecting* 29, 853-882.
- Hirata T, Satoh T & Ito K (1987) Fractal structure of spatial distribution of microfracturing in rock, *Geophys. J. R. astr. Soc.* 90, 369-374.
- Kwiatek G, Saarno T, Ader T, Bluemle F, Bohnhoff M, Chendorain M, Dresen G, Heikkinen P, Kukkonen I, Leary P, Leonhardt M, Malin P, Martinez-Garzon P, Passmore K, Passmore P, Valenzuela S & Wollin C (2019). Controlling fluid-induced seismicity during a 6.1-km-deep geothermal stimulation in Finland, *Science Advances*, 5/5, eaav7224 DOI: 10.1126/sciadv.aav7224
- Lacazette A, Vermilye J, Fereja S & Sicking C (2013) Ambient fracture imaging: A new passive seismic method, SPE 168849 / URTeC 1582380.

- Landro M (2014) A practical equation for air gun bubble time period including the effect of varying sea water temperature; DOI: 10.3997/2214-4609.20141239.
- Leary PC (2002) Fractures and physical heterogeneity in crustal rock. In *Heterogeneity of the Crust and Upper Mantle – Nature, Scaling and Seismic Properties*; Goff JA & Holliger K, Eds.; Kluwer Academic/Plenum Publishers: New York, NY, USA, 2002; pp. 155–186.
- Leary P, Malin P & Niemi R (2017) Fluid flow & heat transport computation for power-law scaling poroperm media, *Geofluids*, Volume 2017, <https://doi.org/10.1155/2017/9687325>.
- Leary P, Malin P, Saarno T & Kukkonen I (2018)  $\alpha\phi \sim \alpha\phi_{crit}$  – Basement rock EGS as extension of reservoir rock flow processes, 43<sup>rd</sup> Workshop Geothermal Reservoir Engineering, Stanford University, February 12-14, SGP-TR-213.
- Leary P, Malin P, Saarno T, Heikkinen P & Diningrat Y (2019) Coupling crustal seismicity to crustal permeability—power-law spatial correlation for EGS-induced and hydrothermal seismicity, 44<sup>th</sup> Workshop on Geothermal Reservoir Engineering Stanford University, 11–13 February 2019.
- Leary PC, Malin PE & Saarno T (2020) A physical basis for the Gutenberg-Richter fractal scaling, 45<sup>th</sup> Workshop on Geothermal Reservoir Engineering, Stanford University, 10–12 February 2020.
- Malhotra S, Rijken P & Sanchez A (2018). Experimental Investigation of Propellant Fracturing in a Large Sandstone Block, SPE Drilling & Completion, 33(02), 087–099. doi:10.2118/191132-pa
- Malin P, Leary P, Shalev E, Rugis J, Valles B, Boese C, Andrews J & Geiser P (2015) Flow lognormality and spatial correlation in crustal reservoirs: II—Where-to-drill guidance via acoustic/seismic imaging, Proceedings, World Geothermal Congress 2015, Melbourne, Australia, 19–24 April 2015.
- Malin PE, Leary PC, Cathles LM & Barton CC (2020) Observational and Critical State Physics Descriptions of Long-Range Flow Structures, *Geosciences* 2020, 10, 50; doi:10.3390/geosciences10020050.
- Sanyal SK, Morrow JW, Jayawardena MS, Berrah N, Li SF & Suryadarma (2011) Geothermal resource risk in indonesia – A statistical inquiry, 36th Workshop on Geothermal Reservoir Engineering Stanford University, January 31 - February 2, SGP-TR-191.
- Sicking C, Vermilye J & Yaner A (2016) Pre-drill reservoir evaluation using passive seismic imaging URTeC: 2460524.
- Sicking C, Vermilye J & A. Yaner (2017), Forecasting reservoir performance by mapping seismic emissions, Interpretation, Vol. 5, No. 4; <http://dx.doi.org/10.1190/INT-2015-0198.1>.
- Sigurdsson O (2015) Experimenting with Deflagration for Stimulating Geothermal Wells, Proceedings World Geothermal Congress, Melbourne, Australia, 19-25 April 2015
- Slichter CS (1905) Field measurements of the rate of movement of underground waters, Water-Supply and Irrigation Paper No. 140, Underground Waters 43, United States Geological Survey.
- Telford WM, Geldart LP, Sheriff RE & Keys DA (1984) Applied Geophysics, Cambridge University Press, pp860; \$4.6.
- Wieland CW, Miskimins JL, Black AD & Green SJ (2006) Results of a laboratory propellant fracturing test in a Colton sandstone block, San Antonio, TX, September 24-27, SPE 102907.